Title

THE USE OF MODERN TECHNIQUES FOR THE CHARACTERIZATION OF THE STRUCTURAL AND CHEMICAL PROPERTIES OF SURFACES

Author

Salmeron, M.

Publication Date

1988-06-01

Center for Advanced Materials

CAM

Published as a chapter in **Nuevas Tendencias en Quĭmica Teórica**, Vol. 3, Servicio de Publicaciones del Consejo Superior de Investigaciones Científicas, Madrid, Spain, 1988

The Use of Modern Techniques for the Characterization of the Structural and Chemical Properties of Surfaces

M. Salmeron

June 1988

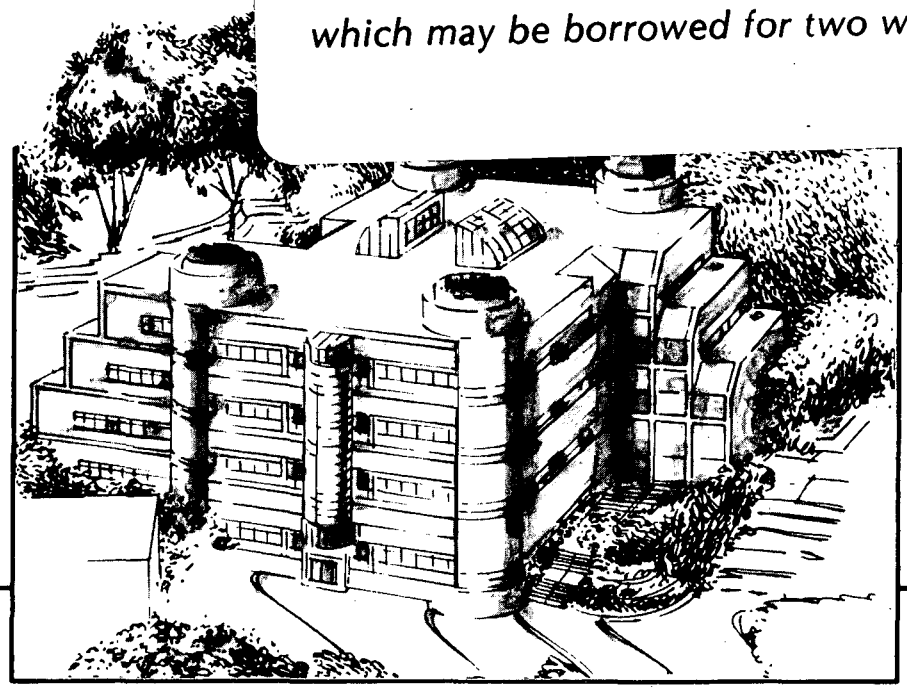

Materials and Chemical Sciences Division

Lawrence Berkeley Laboratory • University of California

ONE CYCLOTRON ROAD, BERKELEY, CA 94720 • (415) 486-4755

Prepared for the U.S. Department of Energy under Contract DE-AC03-76SF00098

DISCLAIMER

LBL-25426

The Use of Modern Techniques for the Characterization of the Structural and Chemical Properties of Surfaces

M. Salmeron

Center for Advanced Materials
Materials and Chemical Sciences Division
Lawrence Berkeley Laboratory
1 Cyclotron Road
Berkeley, California 94720

THE USE OF MODERN TECHNIQUES FOR THE CHARACTERIZATION OF THE STRUCTURAL AND CHEMICAL PROPERTIES OF SURFACES

M. Salmeron
Materials and Chemical Sciences Division
Lawrence Berkeley Laboratory
Berkeley, CA 94720

1. Introduction

Our understanding of surfaces and surface processes has advanced substantially in the last 20 years thanks to the development of techniques that have allowed us to monitor the electronic, geometric, and vibrational structure of surfaces at the atomic level. This development has given birth to the discipline of surface science in the frontier of solid state physics, chemistry, tribology, and electrochemistry, to mention only the most important.

Surface science impacts several areas of vital technological interest that include semiconductors, catalysis, corrosion, and the development of new materials where surfaces play a major role.

When viewed on a microscopic or submicroscopic scale, the surface of a crystal is heterogeneous; various kinds of irregularities are present. Fig. 1 depicts schematically a solid surface. The surface has several different atomic sites which are distinguishable by their number of nearest neighbors or coordination number. There are atoms in terraces where they are surrounded by the largest number of neighbors. There are atoms in steps and at kinks in the steps. These sites have less neighbors than the atoms in the terraces. Adatoms that are located on top of the terrace have, of course, the smallest coordination number.

This model of the solid surface has been utilized to develop the theory of the growth of crystals and to explain the vaporization

mechanisms of solids and other surface phenomena.

The importance of these irregularities and defects at the solid surface in influencing the chemical reactivity has also been established. Early experimental methods for detecting dislocations in solids relied on the different rate of dissolution of a crystal at the point of emergence of dislocations [1]. The decisive role played by steps, kinks, and point defects has also been established in many studies of chemisorption and catalyzed surface reactions [2].

In this paper we will review some of the techniques that have a major impact in our present and future understanding of surfaces. They utilize electrons, ions, and photons as probing particles. We will show how they are applied to specific examples.

2. Techniques and Applications

2.1 Scanning Tunneling Microscope (STM). Is the most recently developed instrument. It permits the study of the topography and electronic properties of surfaces on the atomic scale. This instrument has the additional property of being capable to operate in air, vacuum and liquid environments.

The STM is based on the principle of quantum tunneling of electrons through an energy barrier in the vacuum gap that separates a sharp tip and a conductor surface. At distances of separation of the order of several Angstroms, the wavelength amplitude of the electrons on either side of the vacuum gap has still a non-zero value. Therefore, the electrons can cross the gap and produce, when a non-zero bias voltage is applied between the two surfaces, a measurable tunnel current. A typical value of this current is 1 nA for bias voltages around 1V. The schematic diagram of Fig. 2 illustrates the tunneling phenomenon.

A simple quantum mechanical calculation indicates that the tunnel

current depends exponentially on the separation distance, s, and on the square root of the barrier height, ϕ, as shown in formula (1):

$$(1) \qquad I \propto V_B \times [\exp(-A\phi^{1/2}s)] \times \rho(eV_B)$$

In formula (1) we have also included the density of empty states, $\rho(eV)$, to indicate explicitly that the tunnel probability is proportional to that quantity. A is a constant close to 1. Clearly this expression is an oversimplified description of the real system but illustrates the role of the various parameters that control the tunnel current.

Because of the exponential dependence on the barrier height, only electrons in a narrow energy range near the Fermi level will tunnel from the negative side (the sample in Fig. 2) to the positive side of the barrier with high probability.

Formula (1) shows also that the conductivity I/V_B is proportional to the density of empty states, $\rho(eV_B)$, at fixed distance, s. It also shows that the derivative of the logarithm of I is proportional to $\phi^{1/2}$. This is the base for the operation of the STM in the spectroscopic and local "work function" modes. The use of the term "work function" is misleading since what is actually measured is the local barrier height.

In Fig. 3 we show a schematic of a STM. The metal tip, similar to the tips prepared for Field Ion Microscopy (FIM), is mounted at the vertex of three mutually perpendicular piezoelectric ceramic bars (X, Y and Z).

While the X and Y bars are driven by suitable voltage ramps to cause the tip to raster the surface, the Z bar is biased so that its length is appropriate to maintain a fixed tunnel current value between the tip and the surface. This bias is obtained by a feedback electronic

control circuit as indicated schematically in the figure. The response time of this circuit, τ, is determined by the input resistance and feedback capacitance of the integrator module which constitutes the dominant pole of the circuit. When the X-scanning rate is slower than $1/\tau$, the STM operates in the topographic mode. The images obtained are a collection of lines that delineate the contours of equal charge density at the Fermi level of the sample when it is negatively polarized. With the tip negative, the lines correspond to contours of equal local density of empty states of the sample with energy eV_B above the Fermi level.

When the scanning rate is higher than $1/\tau$, the feedback loop cannot keep the instantaneous value of the tunnel current constant. At high rates only the average height and current are maintained while the instantaneous current changes, reflecting the local tunneling probability. The value of the current versus X and Y constitute the image. This last imaging process is called "current mode."

The two imaging methods are complementary in a way. While large area scans will require slow rates to avoid crashing the tip on local irregularities, small areas of flat surfaces are advantageously imaged in the fast or current mode. Fast scans also minimize thermal drifts of the image. We will show examples of both scanning modes in the following.

The first example corresponds to graphite. This material can be exfoliated to produce atomically clean, ordered surfaces that are inert in air. The image shown in Fig. 4 was taken in air in the current mode. The honeycomb lattice of graphite is easily observed. Notice that three alternating C-atoms in each hexagonal ring are more prominent than the other three. According to Tomanek et al. [3], this is due to the interaction of the p_z orbitals between first and second layer atoms. This interaction disperses the energy of the states associated with these orbitals and, therefore, decreases its density at the Fermi level. Since only three of the atoms have nearest neighbors in the second layer, those will correspond to the weak current points of the image.

In the second example we show in Fig. 5 a "flat" Re(0001) surface, passivated by a saturation layer of sulfur, as seen by the STM, again in air. This surface was prepared in ultra high vacuum (UHV) and its cleanliness and ordering after air exposure was checked by LEED and Auger spectroscopy. The fact that one single atomic layer of sulfur is sufficient to protect the Re surface from oxidation in air is remarkable in itself and provides a hint of why S-containing compounds are good lubricants. In the present case we want to illustrate the presence of numerous steps (single, double, and multiple), kinks and terraces (~1000 Å wide). These types of surface defects cannot be detected by diffraction techniques such as LEED, although as pointed out, it might control the reactivity of the surface.

At higher resolutions, individual sulfur atoms can be imaged also [4,5]. The potential applications of STM to study chemical modifications of surfaces and adsorbates in real conditions of pressure (and in the future also temperature), is only indicated by these examples. This will certainly revolutionize the future research on surfaces for catalysis.

2.2 Low Energy Electron Diffraction. Before the advent of STM, most of our understanding of surface structures was, and still is, obtained from electron and ion spectroscopies. Electron spectroscopies (LEED, AES, XPS, etc.) derive their surface sensitivity from the short inelastic mean free path, λ, of electrons with energies between 10 and a few thousand eV when traveling through a solid material. The curve in Fig. 6 shows the variation of λ with electron energy. As can be seen, between 20 and 1000 eV, $\lambda \simeq 10$Å, indicating that only the first two to three atomic layers are being sampled by techniques utilizing electrons in this energy range.

Low Energy Electron Diffraction (LEED) is a very powerful technique that is utilized extensively to investigate the geometry of single crystal surfaces when clean or when covered with monolayers or adsorbates. In this technique, a beam of monoenergetic electrons is

directed towards the surface where it is diffracted by the two dimensional periodicity of the single crystal target. By measuring the intensity of the diffracted beams as a function of the electron energy, we can obtain the parameters that determine the surface geometric structure; these include bond lengths and bond angles, the position of adsorbate molecules within the unit cell and also atomic displacements of the underlying substrate atoms that occur upon adsorption.

Over the past ten to fifteen years there have been a great number of low-energy electron diffraction studies carried out in many research laboratories to determine the structure of clean solid surfaces and that of adsorbed gases. There are several major findings that emerge from these LEED studies and these are enumerated below:

Surface reconstruction. Many surfaces have atomic structures that are different from that expected from the projection of the x-ray bulk unit cell. The surface atoms assume new equilibrium positions by out-of-plane buckling or by "relaxing" inward (contraction) that often result in entirely different ordered surface structures [6,7].

Stepped Surfaces. As shown with STM, even the flatest metal surface contains steps. However, its density can be increased considerably by cutting crystal surfaces along high Miller index directions. Stepped surfaces of several metals, semiconductors and oxide surfaces were prepared this way [2]. It appears that ordered steps of one atom in height separated by terraces of low Miller index orientation of the same width, on the average, are the stable surface structures of many high Miller index surfaces of solids, regardless of their chemical bonding. Not all stepped surfaces are stable, however [8]. The (510) surface of platinum, for example, is unstable and upon heating it undergoes faceting into two other surfaces: the (100) and the (210). Thus, studies of the relative structural stability of the various surfaces permits determination of their relative surface free energy (the more stable surfaces having the lower surface free energy).

Adsorbed Monolayers. Over the past 20 years, low-energy electron diffraction studies of monolayers of adsorbates on crystal surfaces have shown that: a) adsorbate monolayers are ordered in most cases, and b) the geometric structure of the molecule-surface complex can be determined by analysis of the intensity versus voltage curves (I(V)) of the diffracted beams. An example of crystallography in two dimensions is the determination of the structure of benzene coadsorbed with CO on Rh(111) surfaces. Three ordered structures exist that depend on the ratio of CO and benzene, adsorbed on the surface. Their vibrational spectrum (obtained by High Resolution Electron Energy Loss Spectroscopy) and corresponding LEED patterns are shown in Fig. 7. By analyzing the intensity variation of the diffraction spots as a function of electron energy, Van Hove et al. [9] determined the position on the surface and the bond lengths of the molecule. The result of their analysis is shown in Fig. 8. Both benzene and CO are centered on hcp-type hollow sites in a compact arrangement. The benzene carbon ring has a spacing of 2.20$\pm$ 0.5Å to the metal surface with six identical Rh-C bond lengths of 2.30$\pm$0.05Å. A possible Kekule distortion is found which yields alternating C-C bond lengths of 1.46$\pm$0.15Å and 1.58$\pm$0.15Å in this structure. The short C-C bonds lie over the top of single metal atoms, while the long C-C bonds form bridges linking pairs of metal atoms.

This Kekule-type distortion is analogous to the result on Pt(111) [10] which also shows small variations between C-C bond lengths for bridge-site adsorption.

A connection can be suggested between these results and the catalytic reactivity of Rh and Pt for benzene reactions. The platinum (111) crystal face is an excellent catalyst for the production of benzene from n-hexane or n-heptane (dehydrocyclization). This is an important reaction that is utilized in petroleum refining to produce high octane gasoline. The Rh(111) crystal face, however, cannot carry out this catalytic reaction because of the rapid fragmentation of benzene on the metal surface (hydrogenolysis) under the reaction conditions. It would

be tempting to correlate the surface structures that adsorbed benzene forms on these two transition metal surfaces to their catalytic behavior. Perhaps the large Kekule distortion of the adsorbed aromatic molecule observed in one of the structures on rhodium is indicative of preferential C-C bond breaking to produce CH and C_2H fragments, which occurs as the temperature is increased. Benzene chemisorbed on the Pt(111) crystal face is less systematically distorted, exhibiting only a more uniform expansion of the ring. Perhaps such a structure is indicative of a benzene intermediate on the metal surface that can desorb intact at the higher temperatures and pressures of the catalytic reaction. Future studies will test further the possible correlation between molecular surface structures and catalytic reaction intermediates.

3. Auger Electron Spectroscopy (AES)

Auger electron spectroscopy is suitable for studying the composition of solid (and liquid) surfaces. Using this technique, one analyzes the energy of the electrons emitted from the sample surface following excitation by a primary beam of electrons of moderate energy (1 to 5 KeV). The spectrum thus obtained contains a number of peaks (the Auger peaks) with energies characteristic of the atomic species present at the surface. Once the energy of the Auger peaks is known for each element, one can determine the composition of any surface qualitatively and also, after calibration using standards, quantitatively.

In the energy range typical of Auger spectra (20 to 1500 eV), only a few atomic layers (1 to 7) can contribute to the observed Auger peak intensities. Thus, AES is a surface selective technique. Its sensitivity is of the order of 1% of a monolayer (ML) (10^{13} atoms/cm^{-2}). In the following we will sketch the basic principles and the experiment of Auger spectroscopy and some of its applications in surface science.

The Auger emission occurs as follows. When an energetic beam of electrons or x-rays (1000-5000 eV) strikes the atoms of a material,

electrons which have binding energies less than the incident beam energy may be ejected from the inner atomic levels. By this process a singly ionized excited atom is created. The electron vacancy thus formed is filled by de-excitation of electrons from higher electron energy states that fall into the vacancy. The energy released in the resulting electronic transition can, by electrostatic interaction, be transferred to still another electron. If this electron has a binding energy that is less than the de-excitation energy transferred to it, it will then be ejected into vacuum, leaving behind a doubly ionized atom. The electron that is ejected as a result of this de-excitation process is called an Auger electron and its energy is primarily a function of the energy level separations in the atom.

Most of the Auger spectroscopy studies of surfaces were carried out for purposes of surface chemical analysis. These analysis have shown that carbon, sulfur and calcium are some of the most common impurities that are segregated to the surface of many high purity materials. They are readily detectable by AES. Later we will show an application of AES in combination with ISS.

4. X-Ray Photoelectron Spectroscopy (XPS)

Whereas AES, among other techniques, is primarily concerned with the identification of the element present at the surface, XPS can be used to determine their oxidation state in addition to their qualitative and quantitative analysis. Excellent review papers have been published on this subject [11] to which the reader is referred for more complete information.

Briefly, the principle of the technique is the excitation of electrons in the atom, molecule or solid by means of x-rays and the energy analysis of the photoelectrons that are emitted into the vacuum. The ejected photoelectrons have a kinetic energy equal to $h\nu - E_B$, $h\nu$ being the photon energy and E_B the binding energy of the electron.

These electrons are analyzed with high resolution energy analyzers of various types (hemispherical, cylindrical mirror, etc.).

The higher energy photons in XPS (around 1 KeV and above) make it possible to excite core level electrons. It is the study of these core level peaks and the chemical shifts experienced by these photoelectrons as a result of changes in the chemical environment that is the basis of the applications of XPS to study chemical modifications. We illustrate next how XPS has been used to study the electronic modifications of Ti ions in oxide deposits on Rhodium [12].

Interest in the composition and structure of submonolayer metal-oxide deposits on metals has developed as a consequence of growing evidence indicating that such deposits influence the adsorptive and catalytic properties of the substrate metal. They constitute models also for the supported metal catalysts.

In the present example we will illustrate how the edges of TiO_x islands, deposited on Rh at submonolayer coverages, undergo preferential reduction by producing Ti^{3+} ions. The presence of Rh is essential for reduction at low pressures, since the reducing agent, H_2 or CO, must first chemisorb on the active surface of the metal. In contrast when an inactive metal like Au is used as a substrate, no reduction is observed. Ti was deposited by evaporation from the pure metal in UHV. Following evaporation the samples were oxidized in 2×10^{-6} torr of O_2 at 753 K for 5 min. In the case of Rh substrates this procedure leads to the formation of surface rhodium oxide, particularly in the uncovered areas. The oxygen, however, can be easily removed from the rhodium metal by dosing the sample with CO followed by heating to 753 K. This process is repeated several times until no more CO_2 desorbs and only the CO desorption peak characteristic of clean Rh is observed. To achieve further reduction, the sample is exposed to 50 torr of H_2 at 753 K for 5 min.

Fig. 9 shows the XPS region around the Ti(2) core levels for a sample with 0.5 ML of titania. Spectrum (1) obtained after oxidation exhibits two peaks centered at 463.6 and 458.5 eV that can be assigned to the $2p_{1/2}$ and $2p_{3/2}$ core levels of Ti^{4+}. CO titration causes some attenuation of the Ti^{4+} peaks and the appearance of a peak at 455.7 eV that is assigned to Ti^{3+} species. A peak at 461.4 eV is assigned to the corresponding Ti^{3+} ($2p_{1/2}$) level. H_2 reduction causes a further decrease of the Ti^{4+} peak intensity and a corresponding increase in the Ti^{3+} peak intensity. Reoxidation returns the titanium to the Ti^{4+} state. Similar changes in the XPS spectra are observed for all titania coverages studied, although the relative intensity changes are larger for the smaller coverages.

The extent of reduction of the titania overlayers as a function of TiO_x coverage is determined from the peak areas associated with Ti^{4+} and Ti^{3+} ions. To this end the experimental spectra are deconvoluted into a set of peaks, assuming a Doniac-Sunjic [13] line shape for each peak. The fitting can be done with four peaks corresponding to the $2p_{1/2}$ and $2p_{3/2}$ core levels of the Ti^{3+} and Ti^{4+} species. An example of the result for θ_{TiO_x} = 0.5 ML is shown in Fig. 9. The dashed lines represent the component peaks and the continuous lines their sum. No oxidation states lower than Ti^{3+} are apparent in these spectra. When the same experiment is repeated with Au substrates, only the Ti^{4+} peak is observed by XPS. No reduction is observed for similar CO and H_2 treatments. This result indicates that these reducing agents adsorb on the active metal but not on the oxide layer.

A plot of the percentage of Ti^{3+} in the overlayer as a function of TiO_x coverage of Rh is given in Fig. 10. After the oxidation step, less than 10% of the Ti is in the 3+ oxidation state, except at coverages below 0.3 ML where the fraction rises to around 10%. Titration with CO results in a substantial increase in the percentage of Ti^{3+} for coverages below 0.25 ML, rising to over 50% for 0.15 ML TiO_x. A similar increase was observed after H_2 reduction. In this case the

Ti^{3+} percentage increases from 20-30% for coverages above 1.5 ML to about 65% at 0.15 ML.

The rapid decrease in the percentage of Ti^{3+} as a function of coverage suggests a preferential concentration of these species at the periphery of the two-dimensional TiO_x islands. It is also evident from results obtained with TiO_x on Au that a prerequisite for reduction of TiO_x is adsorption of the reducing agent on portions of the metal substrate not covered by the oxide. The absence of any evidence for Ti^{3+} ions in the spectra obtained when TiO_x is deposited on Au can be attributed to the inability of Au to chemisorb H_2 or CO. The higher degree of Ti^{3+} obtained following reduction of the TiO_x on Rh samples in H_2, as compared to CO, is probably due to the ability of H atoms to penetrate more deeply into the TiO_x islands.

As shown by Fig. 10, the proportion of Ti present in the 3+ oxidation state increases as the TiO_x coverage decreases, consistent with the view that Ti^{3+} cations are produced by reduction of the perimeter of TiO_x islands. It should be noted that even after exposures to methanation reaction conditions (550 K, 1 atm pressure, H_2:CO ratio of 2:1), there is still a significant proportion of Ti^{3+} and that the proportion of Ti^{3+} increases with decreasing TiO_x coverage.

To illustrate the connection between these surfaces studies and the catalytic properties of the Rh-TiO_2 system, we plot in Fig. 11 the methanation rate of this model catalyst as a function of titania coverage. The comparison between Figs. 10 and 11 allows us to conclude that the promotional effects of TiO_2 on Rh arise from the presence of new sites at the island periphery involving both Rh and Ti^{3+} species.

The proposed mode of interaction is shown below.

Since Ti^{3+} is oxophilic, the acid-base interaction between Ti^{3+} and CO should enhance the dissociation of CO, an essential step in the formation of methane [14].

5. Ion Scattering Spectroscopy (ISS)

ISS is another surface sensitive technique which can be used to study surface composition. In ISS experiments a well-focused ion beam of He+, Ne+, or Ar+ particles with energies between a few hundred eV and several KeV is aimed at the target surface where it is reflected after collisions with lattice and surface impurity atoms. Only the ions reflected at fixed angles are analyzed with an electrostatic energy analyzer. The output of this analyzer is an energy spectrum of the reflected ions and has the appearance of a collection of peaks that corresponds to well-defined energy losses of the ions. The energy scale can be easily converted into a mass scale for the target atoms by using a simple relation deduced from the classsical kinetic energy transfer between two colliding rigid bodies. The reason for the good agreement between the simple theory and the experiment is due to the fact that the energy transferred in a collision (several hundred eV) is much higher than the binding energy of the target atoms (some 10 eV), so that in the collision process they can be considered uncoupled from the lattice. On the other hand, the incident energy is low enough so that the inelastic electronic energy transfers (as opposed to kinematical transfers) are very small.

Because the neutralization process is extremely effective as the ions penetrate into the solid, the ISS is only sensitive to the outermost layer of atoms in the target surface [15].

In the following example we illustrate the use of a combination of techniques, including AES and ISS to the study of the syntering of iron oxide on Pt(111) crystals, induced by alkali metals.

Iron oxide has been chosen as the model system since it has important catalytic properties and has been shown previously to grow ordered for the first monolayer on the Pt(111) surface. Hence, at one monolayer coverage iron oxide has a dispersion of unity in contrast to three-dimensional growth where the dispersion would be lower.

Due to the extreme surface sensitivity mentioned, and at one monolayer coverage of iron oxide on Pt(111), only iron and oxygen are visible by ISS under our conditions (500 eV He+ ions). Thus, any decrease in the iron oxide dispersion will be reflected in the appearance of a Pt substrate signal in the ISS experiment.

The preparation of the monolayer iron oxide consists in the evaporation of submonolayer amounts of Fe, by resistively heating a 0.76 mm diameter tungsten wire wrapped with 0.38 mm diameter iron wire, followed by oxidation in 5×10^{-7} torr oxygen at 830 K. The evaporation of iron is repeated until the 1 ML coverage is achieved [16]. After that, the alkali metal is deposited and oxygen is admitted into the chamber for one minute at a pressure of 5×10^{-7} torr. An increase in the oxygen 510 eV Auger peak, with respect to that of the monolayer iron oxide, shows that the alkali is being oxidized. The amount of alkali is determined by monitoring the attenuation of the Fe(651 eV) peak. One-third attenuation of this peak corresponds to 4 to 5 ML of alkali oxide.

The addition of approximately 4 ML of oxidized sodium, lithium, or potassium to the iron oxide monolayer, at 300 K, produces ISS spectra with only the alkali metal visible as shown in Fig. 12 for the case of sodium. Auger electron spectroscopy exhibits, in all cases, alkali, iron, oxygen, and platinum peaks as shown in the same figure. Thus, ISS detects atoms only in the topmost surface layer, while AES monitors the presence of all the species in the top six layers. The fact that oxygen is observed in AES and not in ISS, in all cases, indicates that the alkali resides in the outermost surface layer.

If the iron oxide monolayer, which has been covered with 4 ML of sodium, is heated to 850 K, and then cooled to 300 K, the ISS exhibits a strong platinum peak, along with a sodium peak as shown in Fig. 13. The resulting AES spectrum shows an increase in the intensity of the Pt and iron peaks, and a factor of two decrease in the sodium peak indicating that about 2 ML of the alkali is now present on the surface. Thus, both ISS and AES show that the sintering of iron oxide has occurred leading towards a less than unity dispersion as shown by the presence of the platinum substrate peak in the ISS spectrum. Further heating to 950 K leaves only about 1 ML of sodium (as seen by AES) and ISS shows no bare Pt. Hence, 1 ML of sodium is not enough to keep the iron oxide sintered, and the iron oxide spreads back over the Pt(111) substrate.

6. Present and Future Directions in Surface Chemistry

The above examples illustrate the power of surface science techniques to study surface processes at the atomic level. Perhaps the major criticism that can be made in the case of catalytic applications is that most of the techniques can only operate under high vacuum conditions. Several investigators have been trying to get around this difficulty by performing reactions on single crystal model catalysts in an environmental cell. This cell can isolate the crystal from the UHV environment after characterization to allow the performance of reactions at high pressures (several atmospheres). The accumulation of reaction products in the cell is monitored by gas chromatography.

The reaction can be interrupted and after pumpdown the cell opened to the UHV environment for further analysis of the catalyst surface structure. The schematic drawing of Fig. 15 illustrates the experimental setup used by the research group of Professor G.A. Somorjai [17].

A better way to study surface phenomena is to perform measurements in situ at high pressure. Several techniques exist or are being developed to that effect. One is the previously discussed STM. Recent

experimental results in the author's laboratory on the S covered Mo(001) [5] open the way to further studies of surface structures in atmospheric pressure of other gases.

Spectroscopic techniques involving photons are the natural way to circumvent the problem associated with high pressure that severely limits the mean free path of particles such as electrons and ions. Infrared spectroscopy can be used to study chemisorption processes at high pressures [18]. As a result of recent improvements in the efficiency of photon optics and detection, Raman spectroscopy is also becoming a powerful surface sensitive tool [19].

Finally, we should mention the phenomena of second harmonic generation (SHG). In this technique non linear processes which occur at interfaces between two media with inversion symmetry, generate photons of frequencies twice that of the impinging photon. SHG is extremely sensitive to the surface or interface and is rapidly developing into a tool of choice for the investigation of both surfaces and buried interfaces for which no other techniques exist [20].

A related technique is the Sum Frequency Generation (SFG) where infrared and visible photons are used to explore the surface. Non linear processes occurring in non-centrosymmetric sites will generate new photons with frequencies equal to the sum and difference of the two frequencies. The advantage of SFG is that it carries more direct spectroscopic information of the species adsorbed at the interfaces [21].

During the last twenty years of intense growth, surface science has provided us with a substantial understanding of many fundamental questions concerning the structure of clean and adsorbate covered surfaces. At present it appears that with the rapid development of a new host of techniques, we are ready for a second era of development that will encompass such fields as high pressure environments, liquid phases and even biological materials.

Acknowledgment

This work was suported by the Director, Office of Energy Research, Office of Basic Energy Sciences, Materials Division of the U.S. Department of Energy under Contract No. DE-AC03-76SF00098.

Figure Captions

Fig. 1 Model of heterogeneous solid surface depicting different surface sites. These sites are distinguishable by their number of nearest neighbors.

Fig. 2 Schematic diagram illustrating the energy levels (vertical scale) as a function of distance across the tip-surface normal involved in the tunneling of electrons through a vacuum gap.

Fig. 3 Schematic diagram of the STM setup and feedback electronic circuit.

Fig. 4 Unfiltered current image of the basal plane of graphite in air. The hexagonal honeycomb is clearly visible.

Fig. 5 STM image of a 5000 x 5000 Å area of Re(0001) passivated by a saturation monolayer of sulfur. Mono- and multiple atomic height steps can be observed. Terrace width is 1000 Å average.

Fig. 6 Universal curve for the mean free path of an electron before it undergoes an inelastic collision. (From F.L. Szalkowski, Ph.D. Thesis, University of California-Lawrence Berkeley Lab, 1973, and references therein.)

Fig. 7 LEED patterns and vibrational spectra (High Resolution Electron Energy Loss Spectroscopy) of three coadsorbed CO and benzene layers on Rh(111).

Fig. 8 Adsorption sites and bond lengths of CO and benzene coadsorbed on Rh(11) in a (3x3) periodicity, as deduced from LEED, I(V) analysis.

Fig. 9 XPS spectra of the Ti(2p) region for 0.5 monolayers of TiO_x on Rh. Spectra 1, 2, and 3 were observed after oxidation, CO titration and H_2 reduction of the surface. 4 corresponds to the reoxidation after the treatments indicated.

Fig. 10 Variation of the percentage amount of Ti^{+3} in the TiO_x deposits on Rh as a function of coverage for different sample treatments.

Fig. 11 Methanation rate on TiO_x/Rh as a function of TiO_x coverage. Reaction conditions are 553 K, 1 atm total pressure, and a H_2:CO ratio of 2:1.

Fig. 12 Top: ISS spectrum of 4 monolayers of sodium oxide on top of 1 monolayer of iron oxide on Pt(111).
Bottom: Corresponding Auger spectrum, showing Pt, Fe, O, and Na peaks.

Fig. 13 ISS spectrum of sodium covered iron oxide after heating to 850 K. The presence of an intense Pt peak indicates extensive sintering of the iron oxide monolayer.

Fig. 14 Schematic drawing of an environmental cell in an ultra-high vacuum system for high pressure reactions and pre- or post-examination of the surface with surface science techniques.

References

[1] G.E. Rhead, Surf. Sci., 68, 20 (1977).

[2] G.A. Somorjai, CHEMISTRY IN TWO DIMENSIONS: SURFACES, Cornell University Press, 1981.

[3] D. Tomanek, S.G. Louie, H.J. Mamin, D.W. Abraham, R.E. Thomson, E. Ganz, and J. Clarke, Phys. Rev. B, 35, 7790 (1978).

[4] B. Marchon, D.F. Ogletree, M. Salmeron, and W. Siekhaus, J. Vac. Sci. & Technol. A, 6, 531 (1988).

[5] B. Marchon, P. Bernhardt, M.E. Bussell, G.A. Somorjai, and W. Siekhaus, Phys. Rev. Letters, 60, 1166 (1988).

[6] T.A. Clarke, R. Mason, and M. Tescari, Surf. Sci., 30, 553 (1972).

[7] J.A. Strozier, D.W. Jepsen, and F. Jona, SURFACE PHYSICS OF MATERIALS, Ed. J.M. Blakely, Vol 1, Academic Press, New York (1975).

[8] D.W. Blakely and G.A. Somorjai, Surf. Sci., 65, 419 (1977).

[9] R.F. Lin, G.S. Blackman, M.A. Van Hove, and G.A. Somorjai, Acta Crys. B. (1987)

[10] D.F. Ogletree, M.A. Van Hove, and G.A. Somorjai, Surf. Sci., 187, 1 (1987).

[11] W.M. Riggs and M.J. Parker, METHODS OF SURFACE ANALYSIS, Ed. A.W. Czanderna, Elsevier, Amsterdam (1975).

[12] M.E. Levin, M. Salmeron, A.T. Bell, and G.A. Somorjai, Surf. Sci., 195, 429 (1988).

[13] S. Doniach and M. Sunjic, J. Phys. C, 3, 285 (1970).

[14] M.E. Levin, M. Salmeron, A.T. Bell, and G.A. Somorjai, J. of Cat., 106, 401 (1987).

[15] E. Taglauer and W. Heiland, Appl. Phys., 9, 261 (1976).

[16] G.H. Vurens, D.R. Strongin, M. Salmeron, and G.A. Somorjai, Surf. Sci. Letters, 199, L387 (1988).

[17] B.A. Sexton and G.A. Somorjai, J. Catal, 46, 167 (1977).

[18] F.M. Hoffmann, Surf. Sci. Reports (1983).

[19] a) D. Kirk Veirs, V.K.F. Chia, and G.M. Rosenblatt, Appl. Optics, 26, 3530 (1987).
b) D. Kirk Veirs, V.K.F. Chia, and G.M. Rosenblatt, Proceedings of the Int'l Conf. on Raman Spectroscopy, Sept. 1988.

[20] H.W.K. Tom, C.M. Mate, X.D. Zhu, J.E. Crowell, T.F. Heinz, G.A. Somorjai, and Y.R. Shen, Phys. Rev. Letters, 52, 348 (1984).

[21] J.H. Hunt, P. Guyot-Sionnest, and Y.R. Shen, Chem. Phys. Letters, 133, 189 (1987).

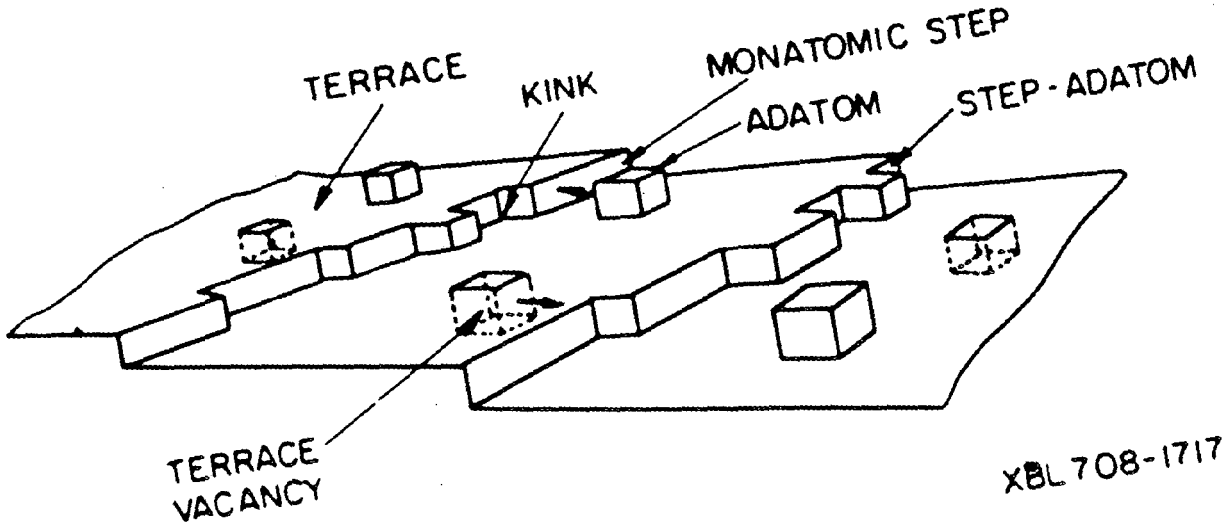
TERRACE
KINK
MONATOMIC STEP
ADATOM
STEP-ADATOM
TERRACE VACANCY
XBL708-1717A

Fig. 1

One-Dimensional Barrier

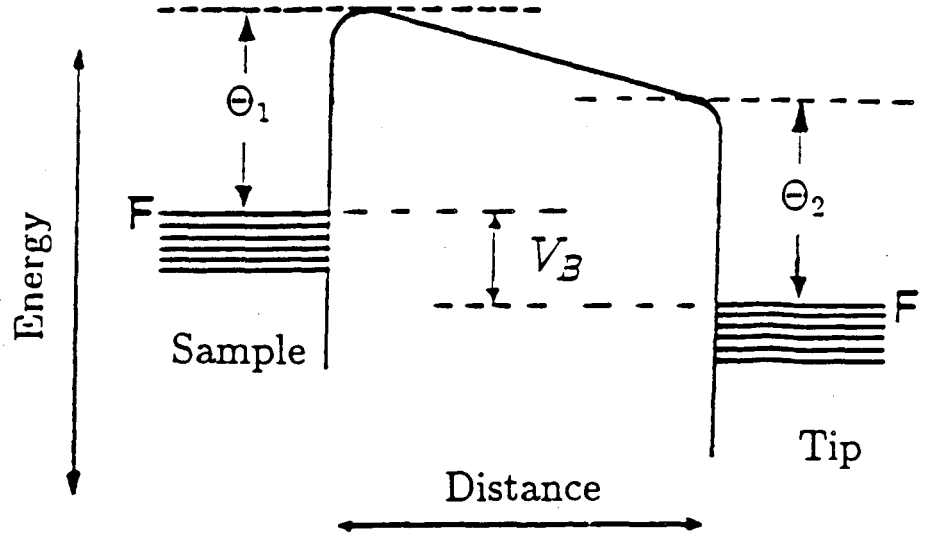

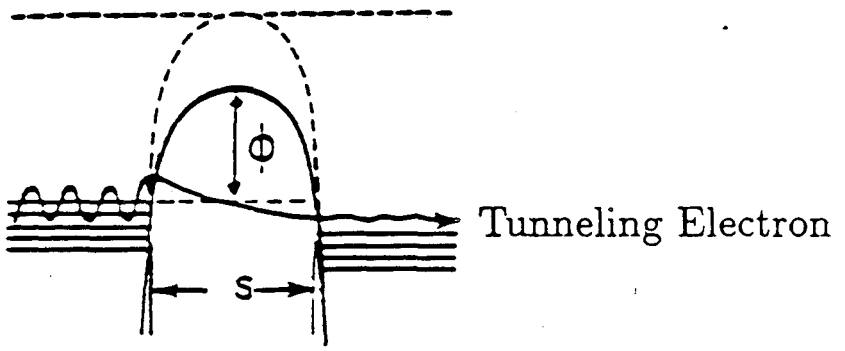

Tunnel Current

XBL 885-1912

Fig. 2

Scanning Tunneling Microscopy

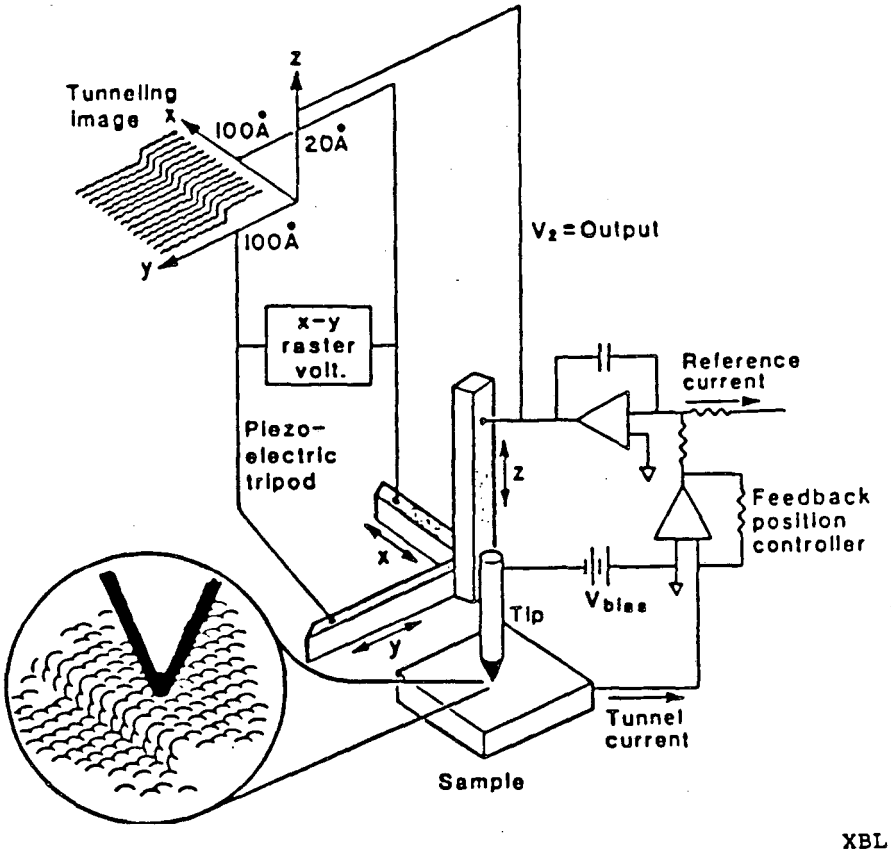

XBL 885-1910

Fig. 3

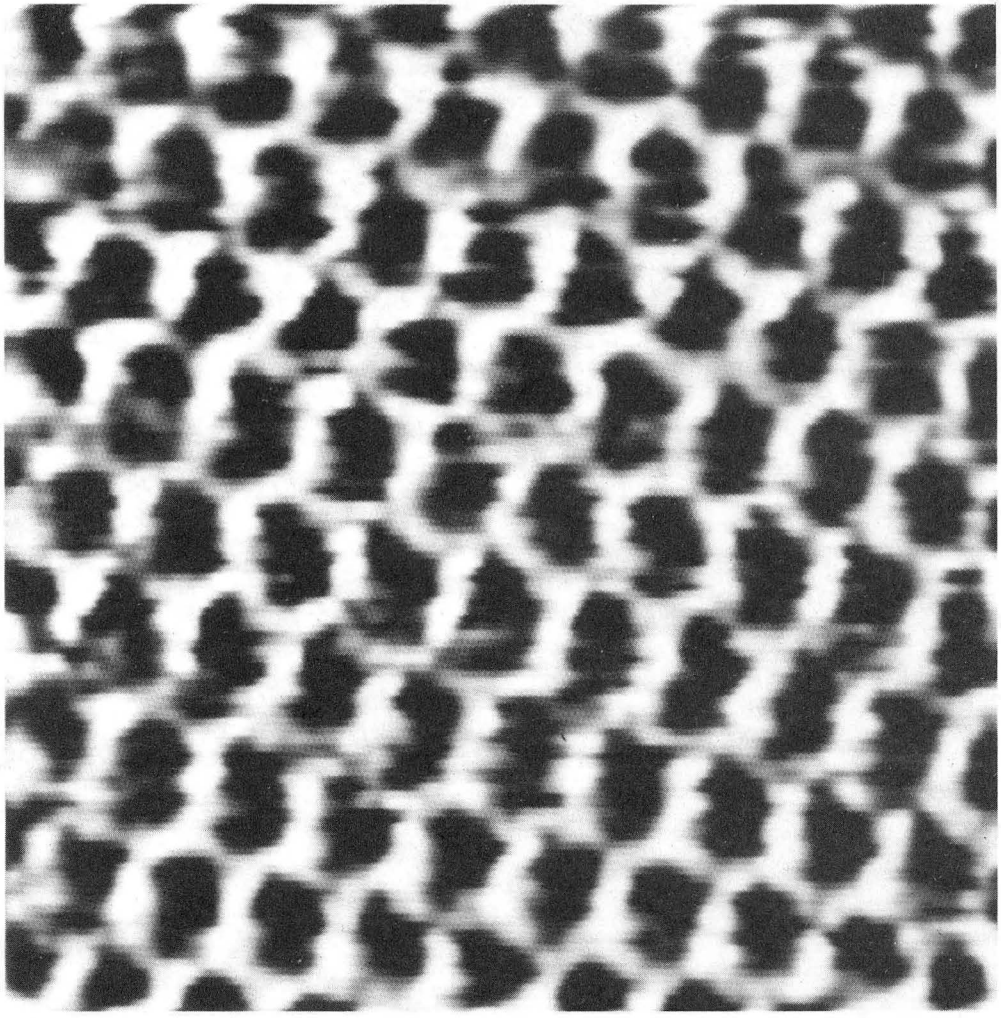

Fig. 4

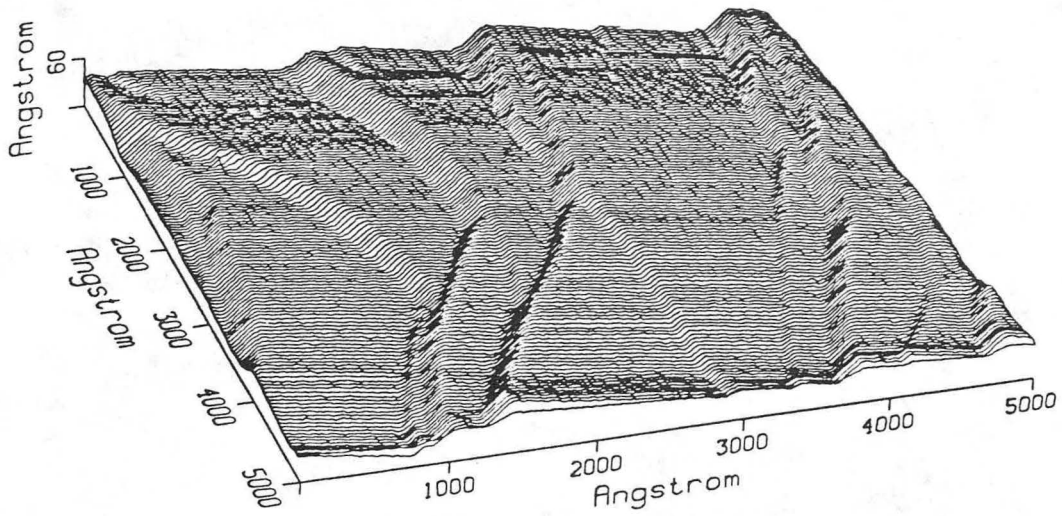

XBL 882-364

Fig. 5

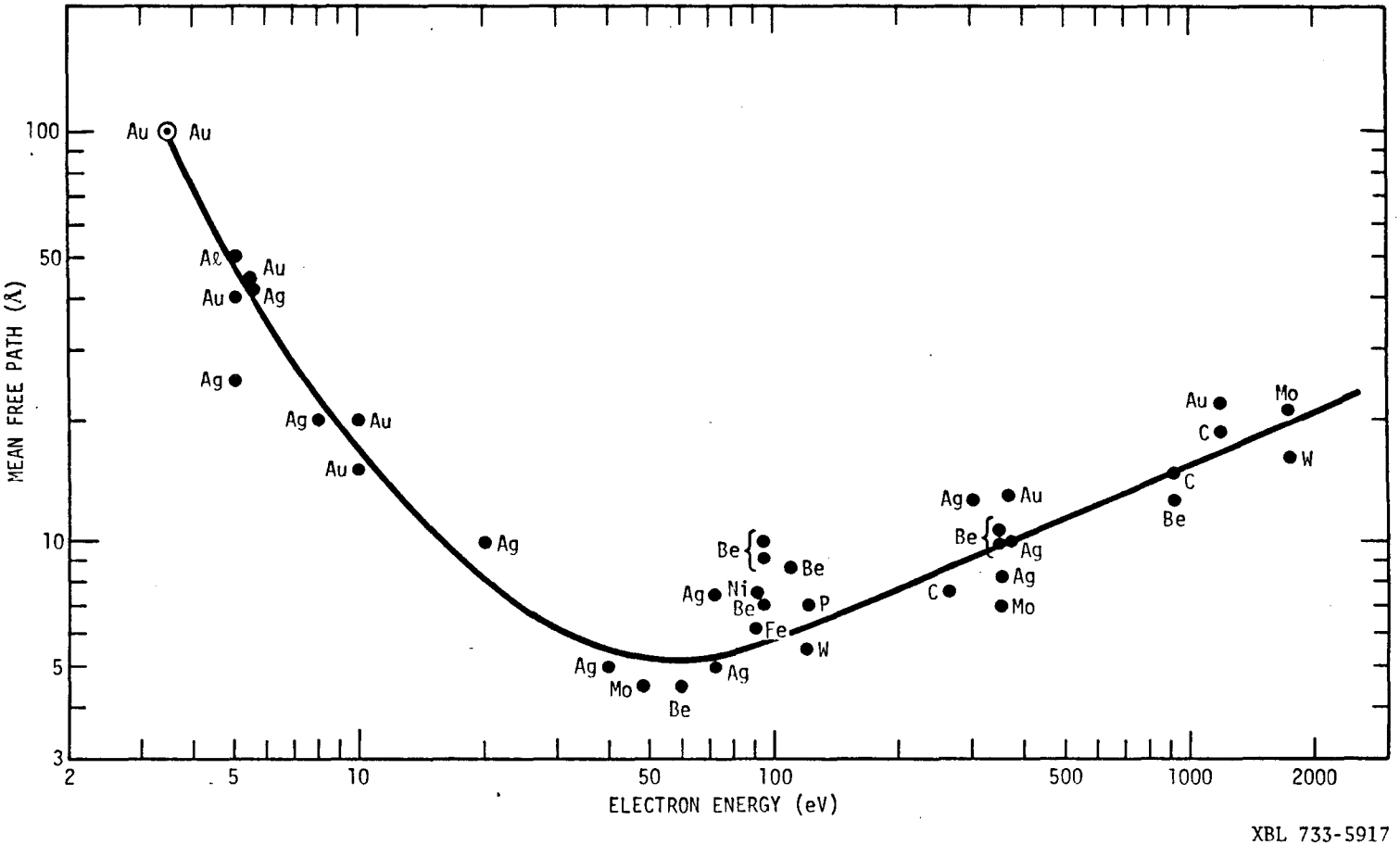
MEAN FREE PATH (Å)
ELECTRON ENERGY (eV)
100
50
10
5
3
2
5
10
50
100
500
1000
2000
Au Au
Aℓ Au
Au Ag
Ag
Ag Au
Au
Ag
Be
Be
Ag Ni
Be P
Fe
W
Ag
Mo
Be
Ag
Ag Au
Be
Ag
Ag
Mo
C
Au
Mo
C
W
C
Be
XBL 733-5917

Fig. 6

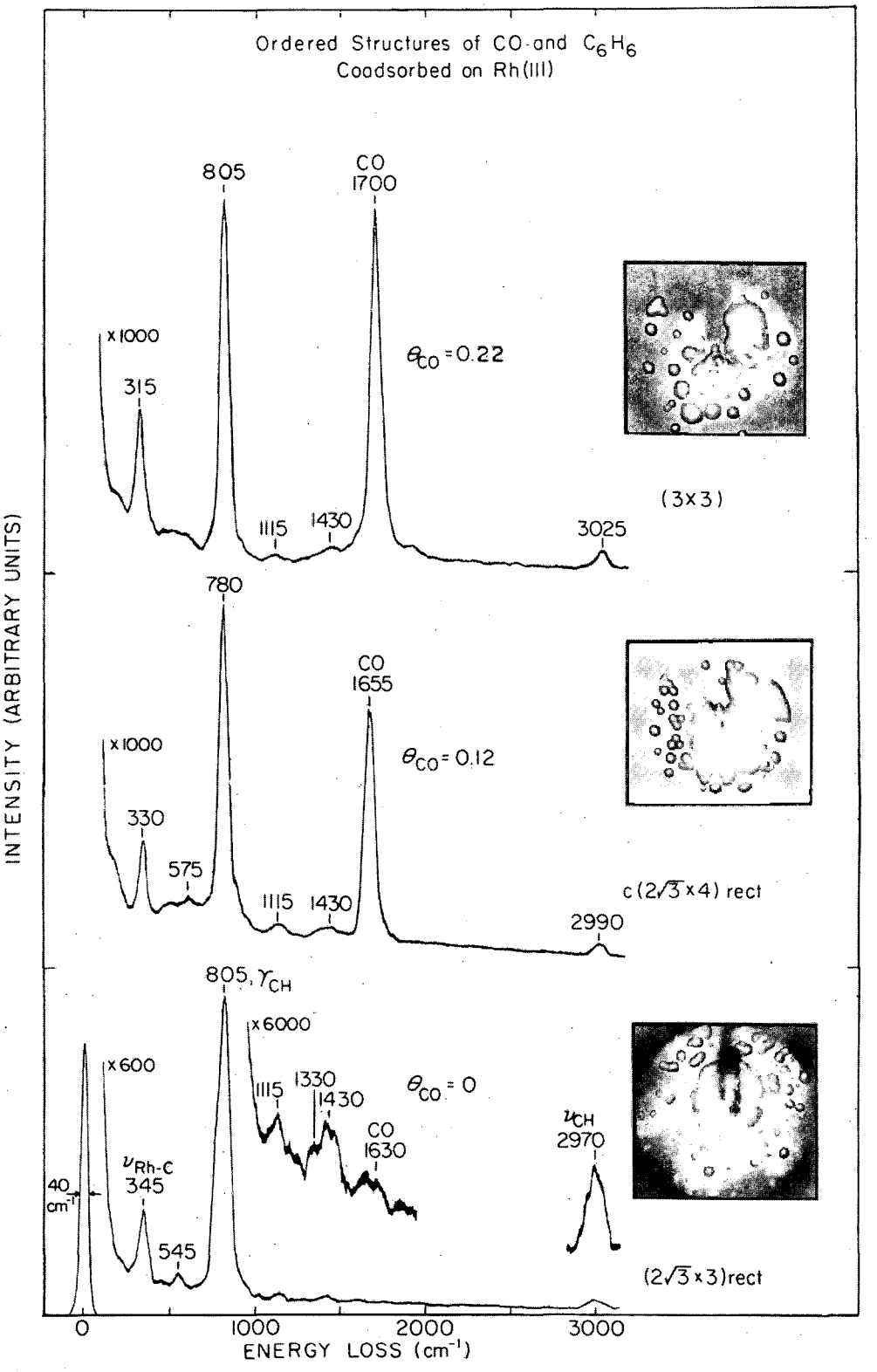
Ordered Structures of CO and C_6H_6
Coadsorbed on Rh(111)
805
CO
1700
x1000
315
θ_{CO} = 0.22
1115
1430
3025
(3x3)
780
CO
1655
x1000
330
575
θ_{CO} = 0.12
1115
1430
2990
c(2√3x4) rect
805, γ_{CH}
x6000
x600
1115
1330
1430
CO
1630
θ_{CO} = 0
ν_{CH}
2970
40 cm⁻¹
ν_{Rh-C}
345
545
(2√3x3)rect
INTENSITY (ARBITRARY UNITS)
0
1000
2000
3000
ENERGY LOSS (cm⁻¹)

Fig. 7

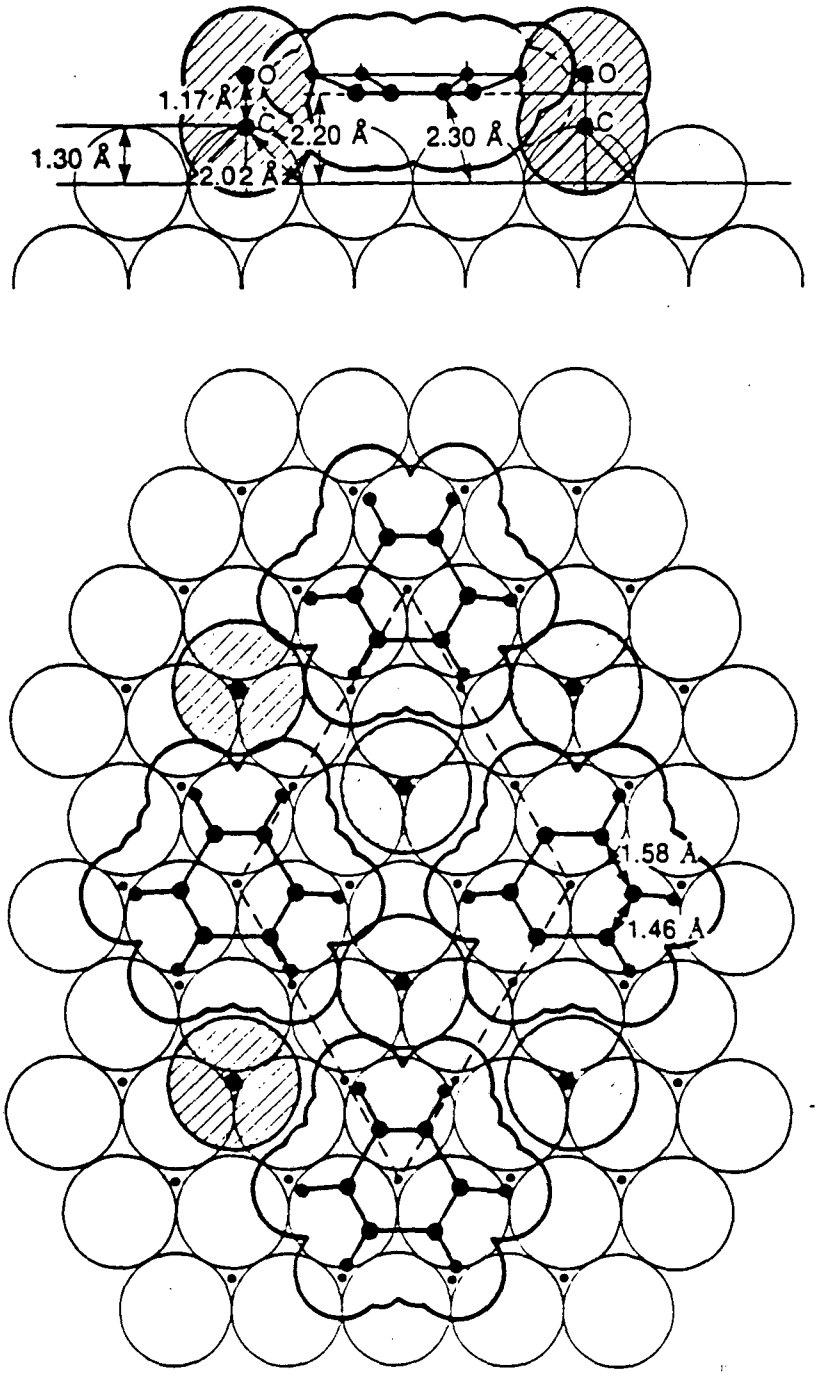

Rh(111) – (3×3) – C_6H_6 + 2CO

XBL 863-10701

Fig. 8

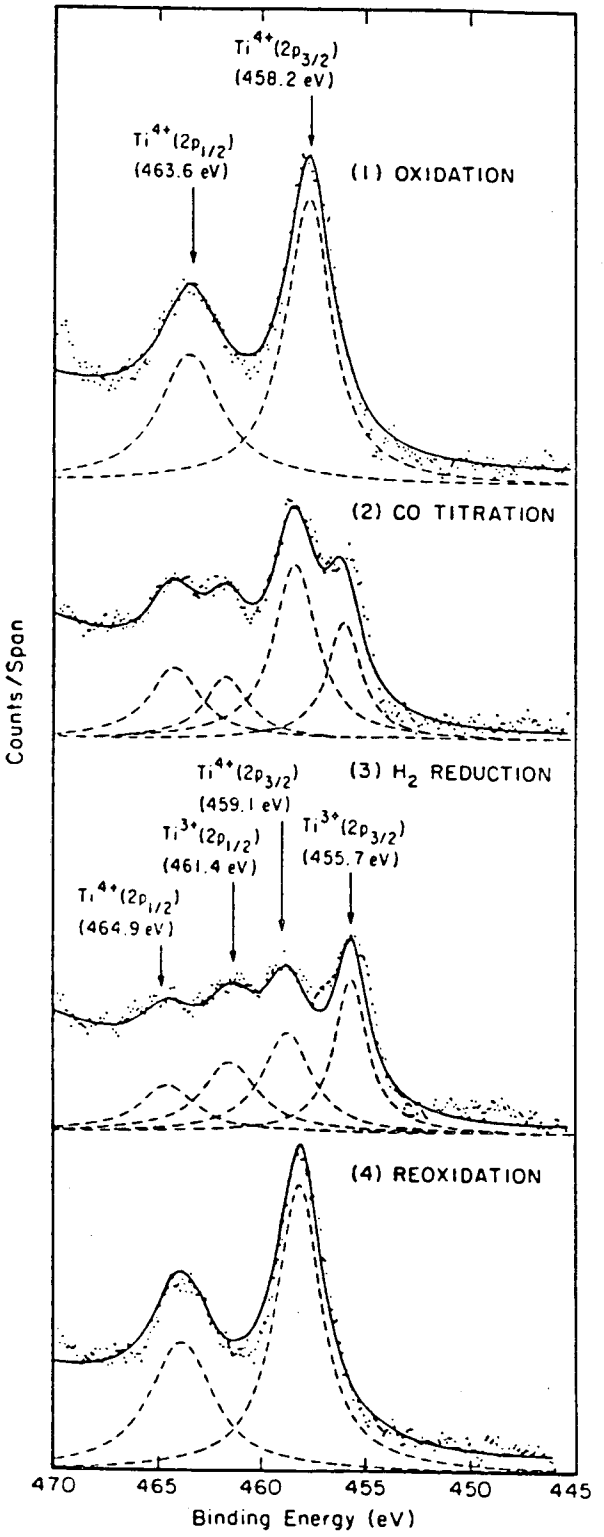

XBL 885-1915

Fig. 9

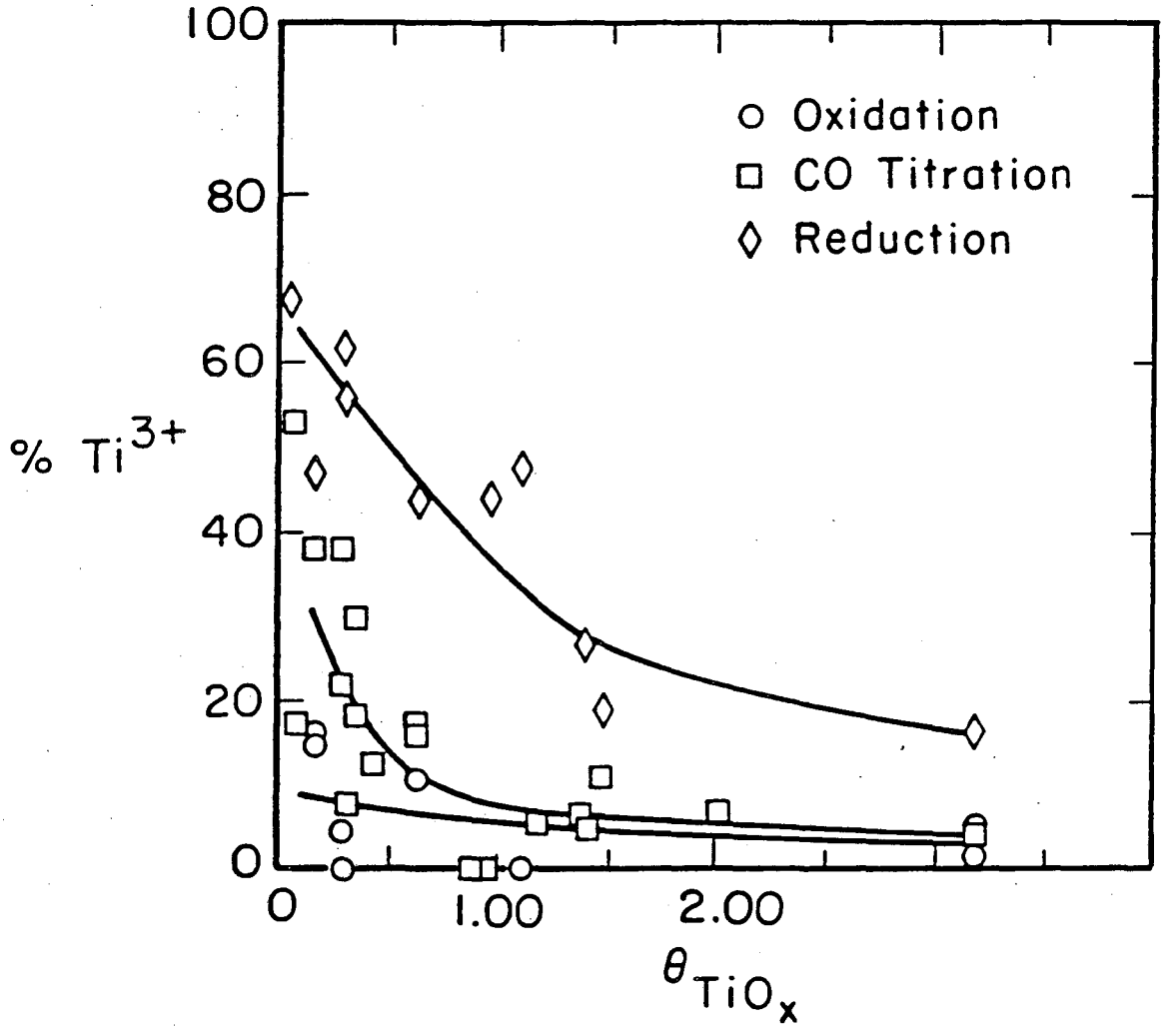

XBL 885-1914

Fig. 10

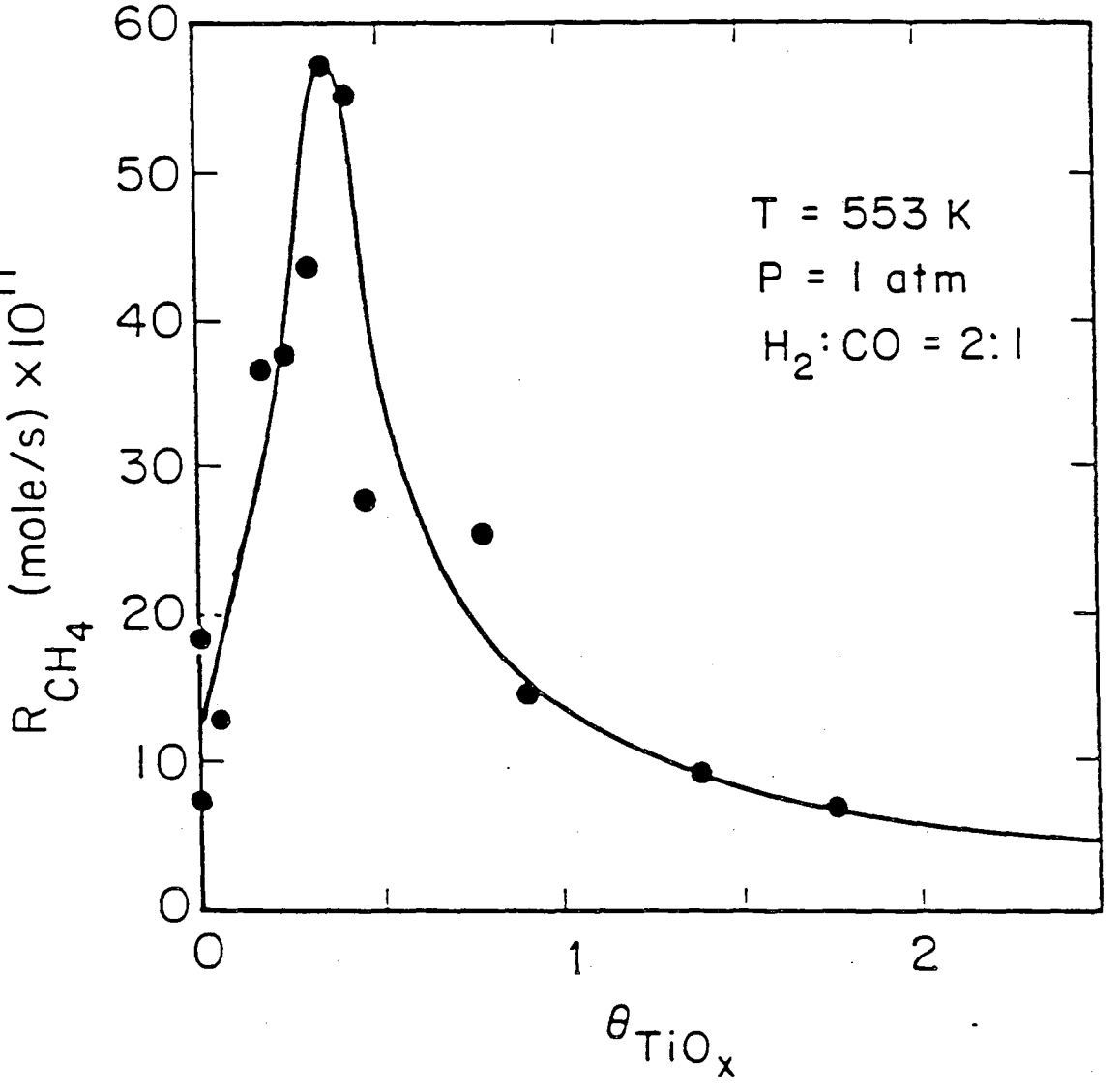

XBL 885-1911

Fig. 11

ISS and AES spectrum of 1 ML Na on FeO_x

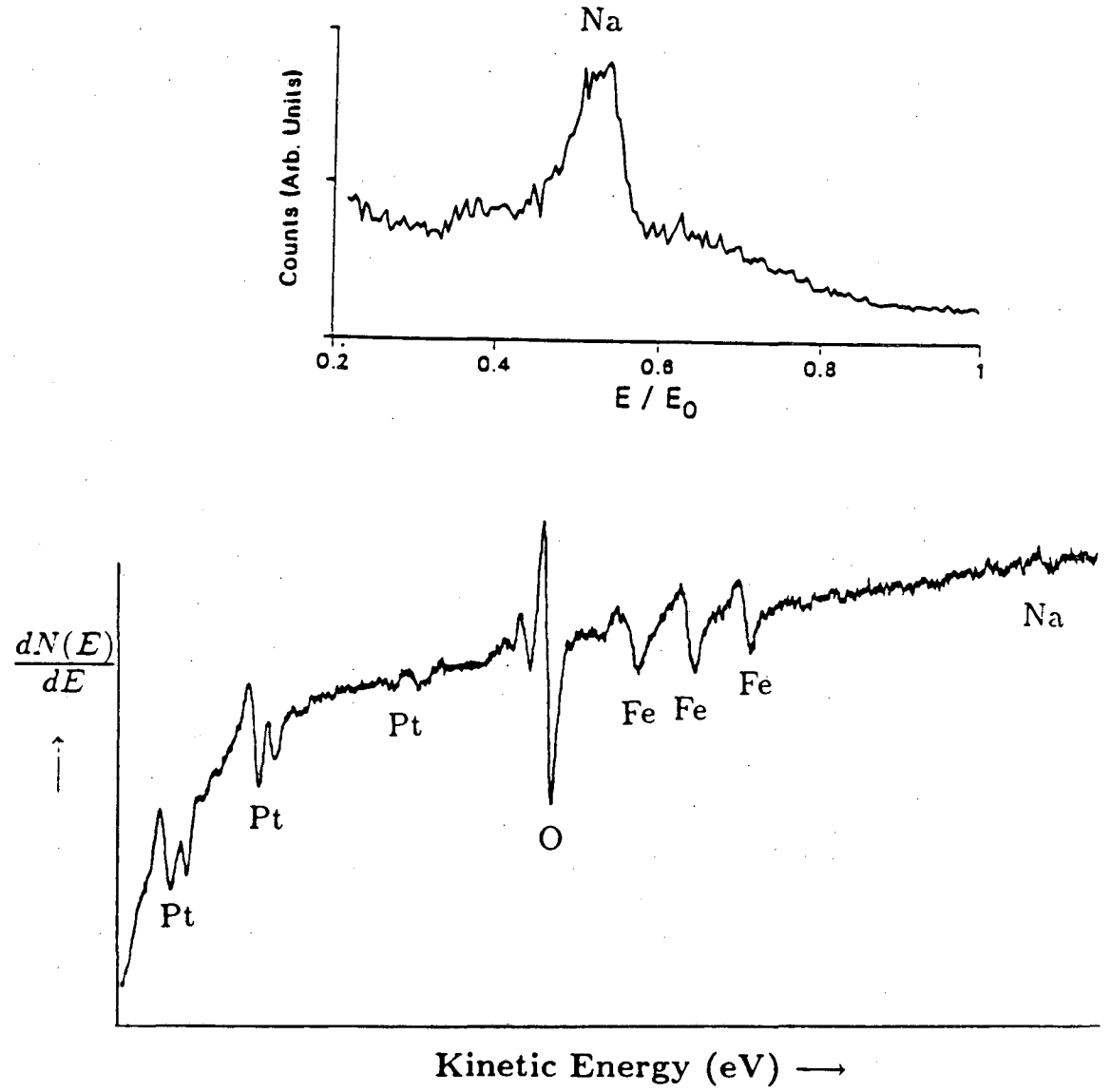

XBL 885-1913

Fig. 12

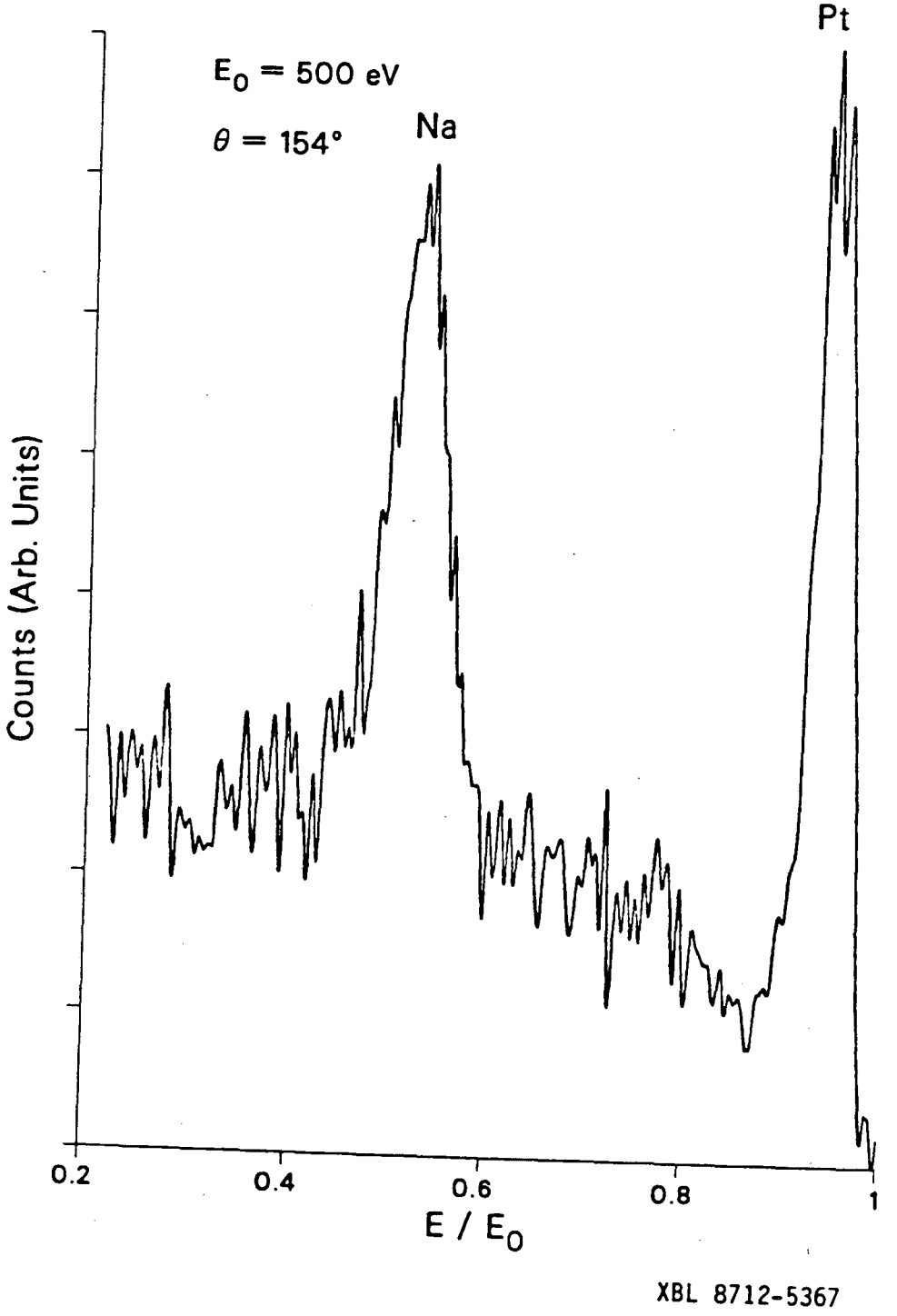
Pt
E_0 = 500 eV
θ = 154°
Na
Counts (Arb. Units)
0.2
0.4
0.6
0.8
1
E / E_0
XBL 8712-5367

Fig. 13

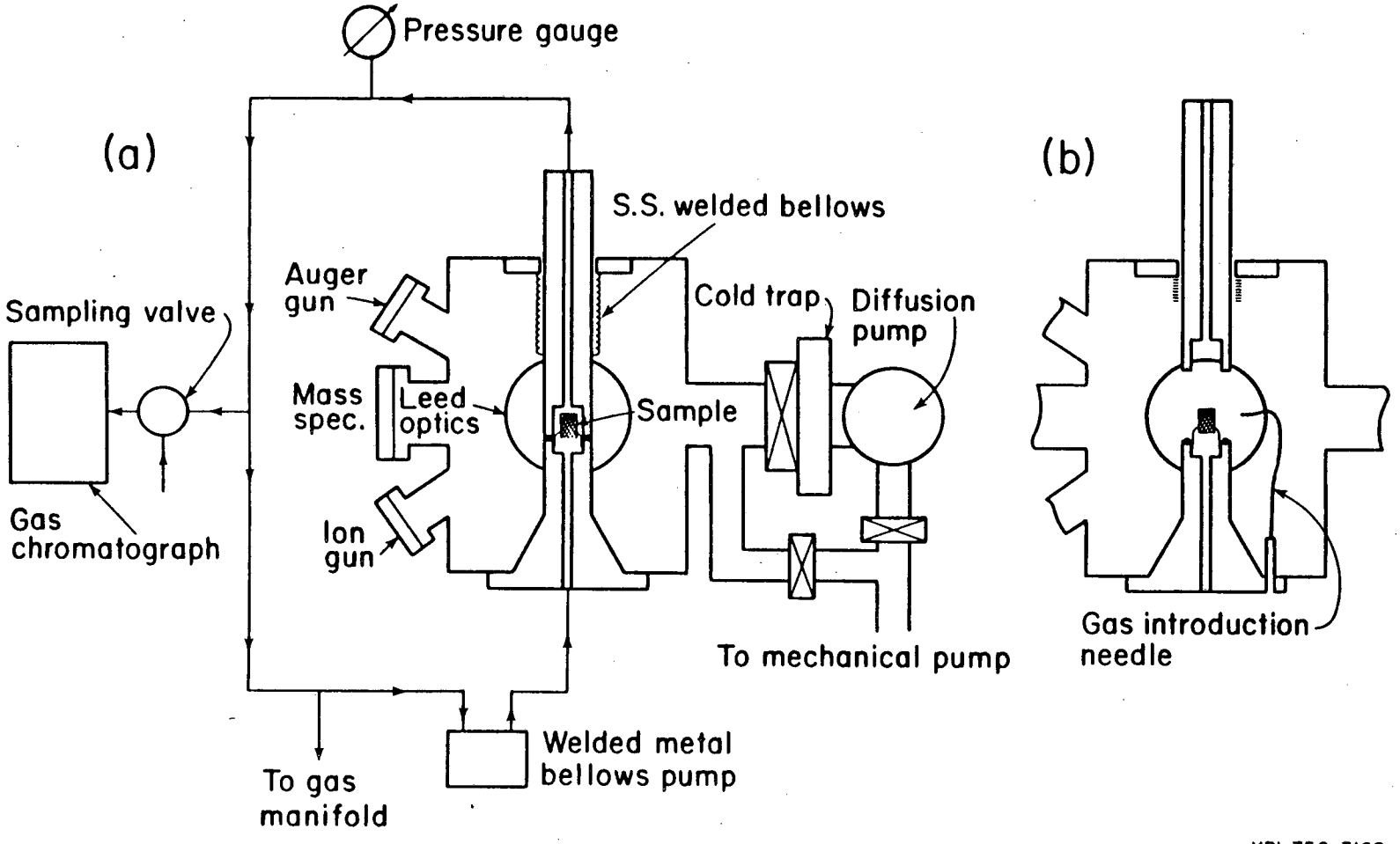
(a)
Pressure gauge
S.S. welded bellows
Auger gun
Sampling valve
Cold trap
Diffusion pump
Mass spec.
Leed optics
Sample
Gas chromatograph
Ion gun
To mechanical pump
Welded metal bellows pump
To gas manifold
(b)
Gas introduction needle
XBL 756-3160

Fig. 14

LAWRENCE BERKELEY LABORATORY
CENTER FOR ADVANCED MATERIALS
1 CYCLOTRON ROAD
BERKELEY, CALIFORNIA 94720